

Article

Facile Synthesis of Bimetallic Pt-Ag/Graphene Composite and Its Electro-Photo-Synergistic Catalytic Properties for Methanol Oxidation

Shuhong Xu ^{1,†}, Lingting Ye ^{2,†}, Zhongshui Li ¹, Yanli Wang ¹, Fengling Lei ¹ and Shen Lin ^{1,*}

¹ College of Chemistry & Chemical Engineering, Fujian Normal University, Fuzhou 350007, China; xushuhongxu@gmail.com (S.X.); zsli@fjnu.edu.cn (Z.L.); yanliwang408@gmail.com (Y.W.); fenglinglei408@gmail.com (F.L.)

² Key Lab of Design & Assembly of Functional Nanostructure, Fujian Institute of Research on the Structure of Matter, Chinese Academy of Sciences, Fuzhou 350002, Fujian, China; ltye@fjirsm.ac.cn

* Correspondence: shenlin@fjnu.edu.cn; Tel.: +86-591-2286-7399; Fax: +86-591-2286-7399

† These authors contributed equally to this work.

Academic Editors: Vincenzo Baglio and David Sebastián

Received: 25 July 2016; Accepted: 9 September 2016; Published: 16 September 2016

Abstract: A Pt-Ag/graphene composite (Pt-Ag/GNs) was synthesized by the facile aqueous solution method, in which Ag⁺ was first transformed into Ag₂O under UV light irradiation, and then Ag₂O, Pt²⁺, and graphene oxide (GO) were simultaneously reduced by formic acid. It was found that Pt-Ag bimetallic nanoparticles were highly dispersed on the surface of graphene, and their size distribution was narrow with an average diameter of 3.3 nm. Electrocatalytic properties of the Pt-Ag/GNs composite were investigated by cyclic voltammograms (CVs), chronoamperometry (CA), CO-stripping voltammograms, and electrochemical impedance spectrum (EIS) techniques. It was shown that the Pt-Ag/GNs composite has much higher catalytic activity and stability for the methanol oxidation reaction (MOR) and better tolerance toward CO poisoning when compared with Pt/GNs and the commercially available Johnson Matthey 20% Pt/C catalyst (Pt/C-JM). Furthermore, the Pt-Ag/GNs composite showed efficient electro-photo-synergistic catalysis for MOR under UV or visible light irradiation. Particularly in the presence of UV irradiation, the Pt-Ag/GNs composite exhibited an ultrahigh mass activity of 1842.4 mA·mg⁻¹, nearly 2.0 times higher than that without light irradiation (838.3 mA·mg⁻¹).

Keywords: platinum; silver; graphene; methanol oxidation; electro-photo catalysis

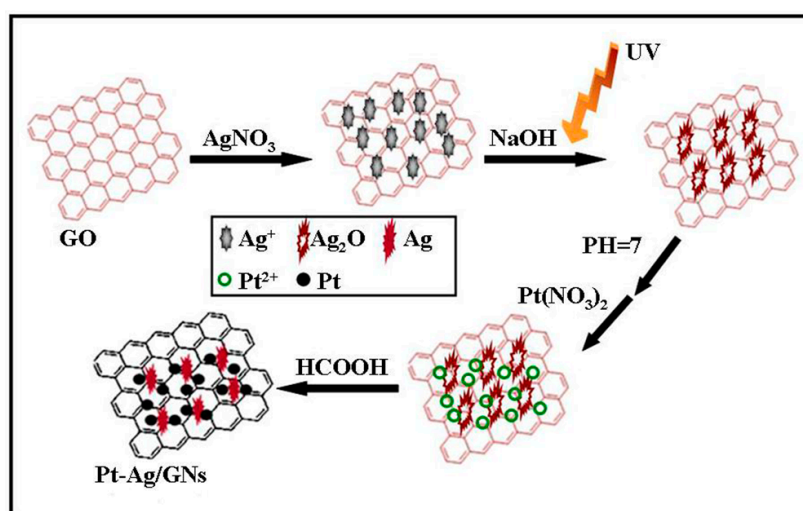
1. Introduction

Platinum has attracted significant attention as a catalyst for the methanol oxidation reaction (MOR) [1]. However, the monometal Pt catalyst is not only expensive, but also easily poisoned by the adsorption of CO-like intermediate species, reducing the electrocatalytic activity of the catalyst during methanol oxidation [2]. Binary or ternary Pt-based catalysts containing other transition metals, such as NiAuPt [3], PtRu [4], PtCu [5], FePt [6], PtSn [7], PtCo [8], PtRhNi [9], or PtPd [10] can evidently improve the performance in catalyzing MOR compared with the monometallic Pt catalysts. Particularly, they can alleviate CO_{ads} poisoning and expose more Pt active sites, resulting in lower noble metal dosages and lower costs. Among the transition metals, Ag can provide rich surface oxygen-containing species to promote the oxidation of CO-like species and prevent the catalyst from poisoning [11]. Ag has a high degree of free electron mobility and exhibits molecular-like excited-state properties with well-defined absorption and emission features, and its surface plasmon resonance (SPR) effect has a prominent contribution to the enhanced photocatalytic activity [12,13]. Therefore, Pt-Ag bimetallic

nano-structures are expected to provide an efficient synergistic effect between the electro-catalytic and photo-catalytic properties for MOR.

The unique properties of graphene nanosheets (GNs), such as larger specific surface areas, excellent optical transmittance, high chemical and thermal stability, and outstanding electrical conductivity, make it a superior support material for Pt-based catalysts [14,15]. Referring to our previously reported catalysts, such as Pt/SnO₂/GNs [16] and Pt/TiO₂/GNs [17], it is known that GNs can not only improve the dispersion of Pt nanoparticles, but also can act as the acceptor and the transfer body of the photo-electron, giving rise to charge transfer and separation efficiency of the photo-generated electron-hole pairs which leads to a better photocatalytic activity.

Herein, we explored a facile method to synthesize Pt-Ag/graphene composite (Pt-Ag/GNs) with the use of formic acid as a reducing agent (Scheme 1). In the synthetic process, HCOOH has the advantages of simple operation, environmental friendliness, and mild reaction conditions, and the Ag₂O intermediate species formed under UV light irradiation contribute to the good dispersion of the bimetallic Pt-Ag nanoparticles on GNs with narrow size distribution. In comparison with commercially available Johnson Matthey 20% Pt/C (denoted as Pt/C-JM) and Pt/GNs, the as-synthesized Pt-Ag/GNs exhibit much higher catalytic activity and stability for MOR and better resistance to CO poisoning. More importantly, with the aid of the integrated photo-response of Ag and GNs, methanol electro-catalytic oxidation and photo-catalytic oxidation reactions are synergistically coupled on Pt-Ag/GNs under UV irradiation or visible light irradiation, bringing about increased catalytic activity and stability.



Scheme 1. Schematic of the preparation procedure of the Pt-Ag/GNs composite.

2. Results and Discussion

Figure 1 shows the XRD patterns for the following samples: (a) Ag/GNs, (b) Pt/GNs and (c) Pt-Ag/GNs. The diffraction pattern for the Pt/GNs catalyst shows the typical peaks of the face centered-cubic (fcc) structure of Pt (0). Peaks are located at 39.8°, 46.3°, 67.6° and 81.4° corresponding to the (111), (200), (220) and (311) planes of Pt (0) [18,19]. This indicates that the reduction of the Pt²⁺ precursor to Pt (0) by formic acid has been effective. Pt-Ag/GNs (curve c) shows broader and asymmetrical peaks in comparison to both Ag/GNs and Pt/GNs. The reason for this is that these peaks are the combination of the peaks for both Pt and Ag, which indicates that both elements are not alloyed. This is also supported by the the Powder Diffraction File of International Centre for Diffraction Data (ICDD PDF) of Pt (No. 04-0802) and Ag (No. 04-0783) in Figure 1. Furthermore, the representative diffraction peaks assigned to the (111) and (220) planes of Ag₂O located at 32.8° and

54.9°, respectively, are not observed (Figure 1) [20], suggesting that the intermediate species Ag₂O was completely transformed into Ag after the reduction with formic acid.

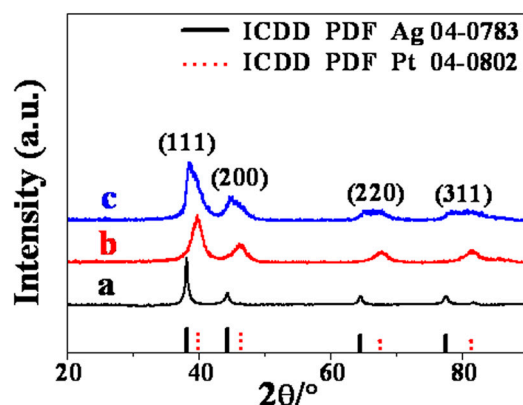


Figure 1. XRD patterns of Ag/GNs (a), Pt/GNs (b) and Pt-Ag/GNs (c).

The morphologies of the Pt-Ag/GNs and Pt/GNs composites were characterized by transmission electron microscopy (TEM) and high-resolution TEM (HRTEM). The TEM image of Pt/GNs shows apparent aggregation of the Pt particles on the surface of GNs (Figure 2A). By contrast, the spherical bimetallic nanoparticles of the Pt-Ag/GNs composite are uniformly dispersed on the surface of the GNs with an average size of about 3.3 nm (Figure 2D,E), and a relatively narrow size distribution peak (the inset of Figure 2E). HRTEM images of Pt/GNs and Pt-Ag/GNs (Figure 2C,F) show lattice fringes with spacing of 0.225 nm, which is in good agreement with the (111) planes of fcc Pt (0) [21]. In addition, the lattice spacing of 0.235 nm shown in Figure 2F can be assigned to the (111) planes of metallic Ag [22], further proving the formation of separate Ag nanoparticles in Pt-Ag/GNs. This also indicates that the Pt and Ag nanoparticles are separately deposited on the GNs, instead of forming a Pt-Ag alloy. The reason for this may be that Ag⁺ was first transformed into Ag₂O under UV irradiation [23], and then the heterogeneous phase between the precursor Pt²⁺ and Ag₂O can prevent the formation of a binary alloy structure, which results in the formation of the heterostructured Pt-Ag nanoparticles. It is worth mentioning that (111) Pt planes are adjacent to (111) Ag planes, suggesting that Ag₂O provides an anchor for the Pt²⁺ precursor during the reduction process, resulting in a proper dispersion of Ag and Pt nanoparticles on the GNs after reduction by formic acid. The morphologies of Pt and Ag nanoparticles on GNs were further analyzed by high-angle annular dark-field scanning transmission electron microscopy (HAADF-STEM) and elemental mapping images. As shown in Figure 3A, Pt and Ag nanoparticles are highly dispersed onto the GNs surface, and it is difficult to discriminate Pt from Ag because of their full integration. Elemental mapping (Figure 3B,C) of the Pt-Ag/GNs composite show that the Pt and Ag nanoparticles are in good co-existence and in intimate contact, which further verifies that Ag₂O provides an anchor for the precursor of Pt²⁺. The selected area electron diffraction (SAED) pattern demonstrates that the Pt-Ag/GNs composite has a typical polycrystalline structure (the inset of Figure 2F).

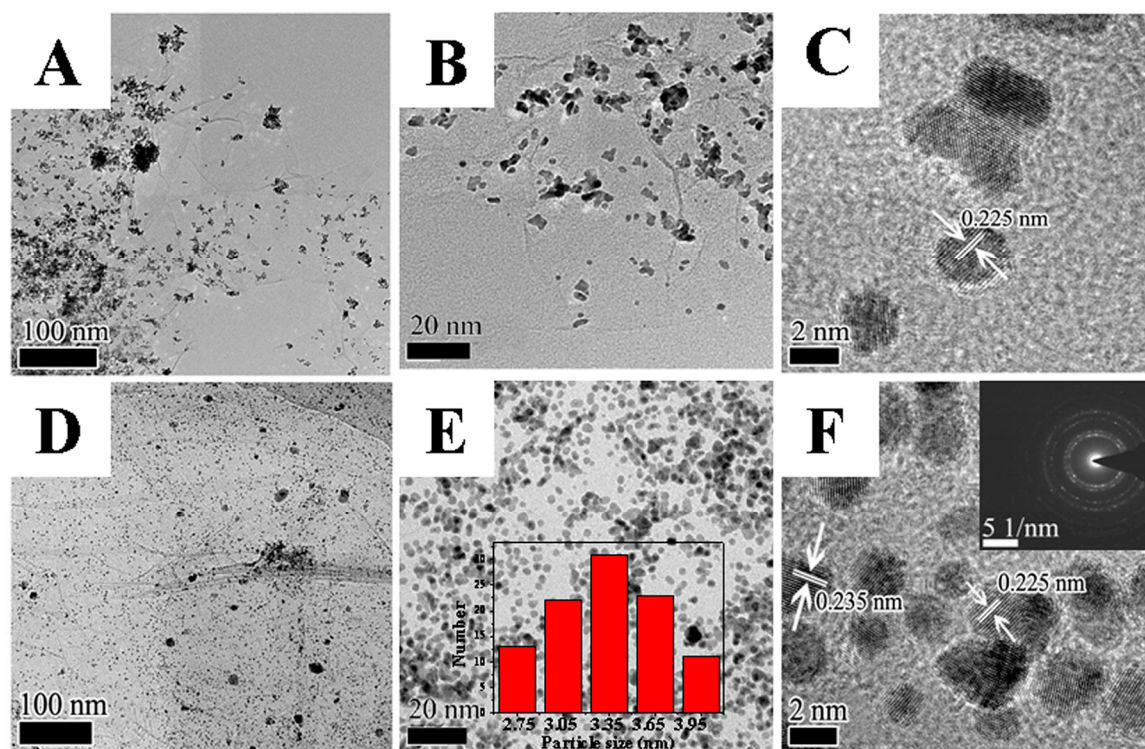


Figure 2. Transmission electron microscopy (TEM) and high-resolution TEM (HRTEM) images of Pt/GNs (A, B, C) and Pt-Ag/GNs (D, E, F); particle size distributions of Pt-Ag/GNs in the inset of (E); SAED of Pt-Ag/GNs in the inset of (F).

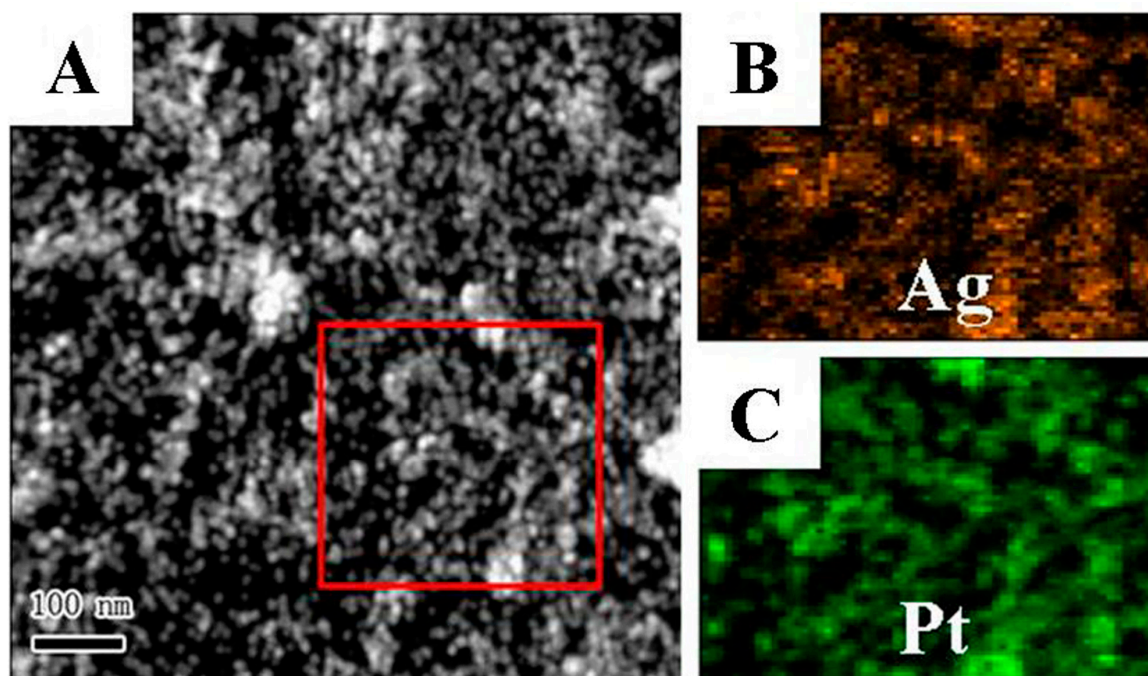


Figure 3. High-angle annular dark-field scanning transmission electron microscopy (HAADF-STEM) images for Pt-Ag/GNs (A); elemental mapping images for Ag (B) and Pt (C).

X-ray photoelectron spectra (XPS) were used to further analyze the valence states and surface composition of the as-synthesized composites, displayed in Figure 4. The binding energies of Ag 3d_{5/2}

and Ag $3d_{3/2}$ for Pt-Ag/GNs are 368.1 eV and 374.0 eV (Figure 4A), respectively, demonstrating that the deposited Ag nanoparticles are in a zero-valent state [22,24]. Figure 4B shows Pt 4f spectra of Pt/GNs (curve a) and Pt-Ag/GNs (curve b). The peaks located at 71.08 and 74.38 eV for Pt-Ag/GNs and at 71.38 and 74.79 eV for Pt/GNs can be assigned to the binding energies of Pt $4f_{7/2}$ and Pt $4f_{5/2}$, respectively. Their values are in line with that of platinum in the zero-valent state, which further verifies the formation of Pt (0) nanoparticles in Pt/GNs and Pt-Ag/GNs composites [14]. However, the binding energy of Pt 4f for Pt-Ag/GNs is significantly lower than that for Pt/GNs. The reason may be that Pt has a higher electro-negativity than Ag, so Pt can withdraw electrons from the neighboring Ag atoms [25]. Furthermore, there exists an electrostatic interaction between the metal nanoparticles and the graphene sheets because of the remaining oxygen containing functional groups on the surface of the GNs, which allows a high dispersion of Pt-Ag nanoparticles on GNs to produce stronger electronic interactions between metal nanoparticles and supports [26,27], inducing their binding energy shift.

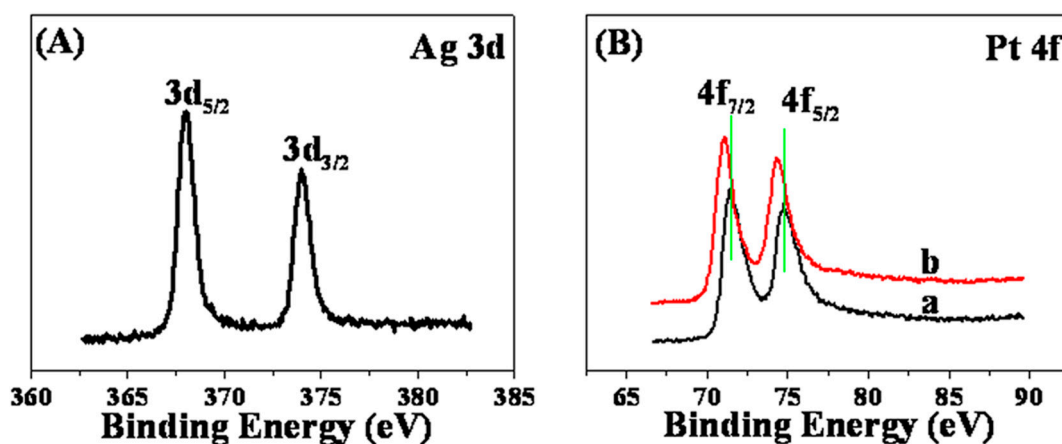


Figure 4. (A) Ag 3d X-ray photoelectron spectra (XPS) profile of Pt-Ag/GNs; (B) Pt 4f XPS profiles for Pt/GNs (a) and Pt-Ag/GNs (b).

Raman spectra were used to discuss the structural changes of the graphene based composites during the preparation process. As shown in Figure 5, the D band (associated with a breathing mode of k-point phonons of A_{1g} symmetry) and the G band (corresponding to the E_{2g} phonon of the C sp^2 atom) are observed [28]. I_D/I_G , namely the intensity ratio of the D and G bands, can be used to predict the extent of defects in carbonaceous materials [29]. It is found that the I_D/I_G value of the Pt-Ag/GNs composite (curve b) is obviously smaller than that of Pt/GNs (curve a), which indicates that there is a lower degree of disorder for the graphene structure.

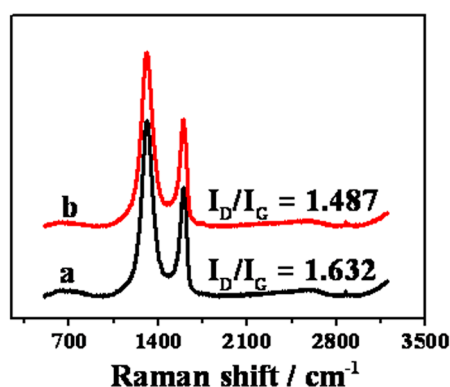


Figure 5. Raman spectra of Pt/GNs (a) and Pt-Ag/GNs (b).

Cyclic voltammograms (CVs) of Pt/C-JM (curve a), Pt/GNs (curve b) and Pt-Ag/GNs (curve c) in a 0.5 M H₂SO₄ solution were collected to evaluate the electrochemical properties of the different composites, shown in Figure 6. In general, the hydrogen adsorption/desorption peaks of the CV curves can be utilized to measure the electrochemically active surface area (ECSA) of Pt-based catalysts on the basis of Equation (1) [30].

$$\text{ECSA} = Q_{\text{H}} / (210 \mu\text{C} \cdot \text{cm}^{-2} \times \text{Pt loading}) \quad (1)$$

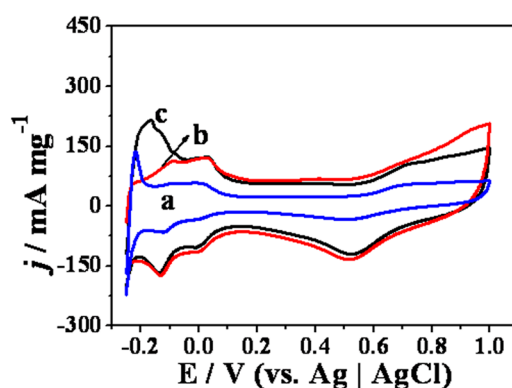


Figure 6. Cyclic voltammograms (CVs) of Pt/C-JM (a), Pt/GNs (b) and Pt-Ag/GNs (c) in 0.5 M H₂SO₄; scan rate: 100 mV·s⁻¹.

The ECSA values for the Pt-Ag/GNs (curve c) is 120.3 m²·g⁻¹, which is about 1.5 times and 2.5 times higher than that of the Pt/GNs (curve b) (80.5 m²·g⁻¹) and the Pt/C-JM (curve a) (48.9 m²·g⁻¹), respectively. The larger ECSA mainly arises from better dispersion of the Ag and Pt nanoparticles on the GNs (as shown in TEM analysis), which can offer more active sites.

In order to further investigate their catalytic activities for methanol oxidation reaction (MOR), CVs in 1 M CH₃OH + 0.5 M H₂SO₄ solution were conducted (Figure 7). As shown in Figure 7, all of the curves have two significant oxidation peaks: the forward scan oxidation peak is assigned to the peak current of methanol oxidation, and the reverse scan oxidation peak is attributed to the peak current of the CO intermediate species oxidation. As presented in Figure 7, the forward scan current density (mass activity) increased up to 838.3 mA·mg⁻¹ on Pt-Ag/GNs without light irradiation (*t* = 0 min), which is significantly higher than that of Pt/GNs (653.8 mA·mg⁻¹) and Pt/C-JM (402.6 mA·mg⁻¹). The improved catalytic activity may originate from the role of Ag. First, the introduction of Ag into Pt-Ag/GNs brings about the good distribution of the Ag and Pt nanoparticles on the GNs, which generates more active sites for MOR (as shown in Figure 6). Secondly, Ag has a lower electro-negativity than Pt, so Pt can withdraw electrons from the neighboring Ag atoms, which produces stronger electronic interactions between the Pt and Ag nanoparticles (as analyzed in the Pt 4f spectra) [25]. The interaction may effectively weaken the capacity to bind to adsorbed intermediates of Pt [31]. Thirdly, the coexistence of Ag and Pt nanoparticles on the surface of GNs can increase the electron transfer efficiency via an interfacial interaction among the Ag, Pt and GNs, which was verified by Electrochemical Impedance Spectra (EIS) analysis. As shown in Figure 8, the Nyquist plots of EIS for Pt-Ag/GNs, Pt/GNs and Pt/C-JM were obtained in 0.5 M H₂SO₄ + 1.0 M CH₃OH solution at 0.5 V. The diameter of the primary semicircle can be used to analyze the charge transfer resistance of the catalyst, which describes the rate of charge transfer during the methanol oxidation reaction [32]. The semicircle radius of Pt-Ag/GNs (curve c) is much smaller than that of Pt/GNs (curve b) and Pt/C-JM (curve a), which illustrates that Pt-Ag/GNs have better charge transfer and a faster methanol oxidation reaction rate [33,34].

Most interestingly, it was found that the peak current value of the Pt-Ag/GNs composite was significantly increased under UV or visible light irradiation. Particularly, the Pt-Ag/GNs composite exhibited a remarkably increased value (about $1842.4 \text{ mA}\cdot\text{mg}^{-1}$) after UV irradiation for 30 min, which is nearly 2.0 times higher than that without light irradiation ($838.3 \text{ mA}\cdot\text{mg}^{-1}$) (Figure 7A). The value is also far more than that of reported commercial PtRu-C (E-TEK, Secaucus, New Jersey, NJ, USA) [35] or PtRu-C prepared by the ethanol reduction method [36]. However, the current density of Pt/GNs and Pt/C-JM are only slightly increased (Figure 7B,C). The obvious improvement in the catalytic activity of Pt-Ag/GNs under external light irradiation apparently stem from the introduction of Ag, which may endow Pt-Ag/GNs with an efficient electro-photo synergistic catalysis for MOR under UV or visible light irradiation. In order to further check whether the Pt-Ag/GNs composite can effectively respond to ultraviolet light or visible light irradiation, chronoamperometric curves of Pt-Ag/GNs were measured by turning on/off UV or visible light every 10 s in 1 M CH_3OH + 0.5 M H_2SO_4 solution (presented in Figure 9). When UV or visible light was turned on, the current density increased rapidly and temporarily up to a steady state; as the light was turned off, the current density decreased instantly. In the first illumination cycle, the current intensities were boosted from 0.325 to 2.171 ($\text{mA}\cdot\text{cm}^{-2}$) (568.0% increase) under UV irradiation (curve c) and from 0.325 to 1.522 ($\text{mA}\cdot\text{cm}^{-2}$) (368.3% increase) under visible irradiation, respectively (curve b). The increase of current density in the first illumination cycle is apparently higher than that of the reported silicon-based Pt-Ag nano-forests catalyst under visible irradiation [37]. Therefore, the as-synthesized Pt-Ag/GNs should be a more efficient Pt-Ag bimetal electro-photo synergistic catalyst for MOR under solar irradiation.

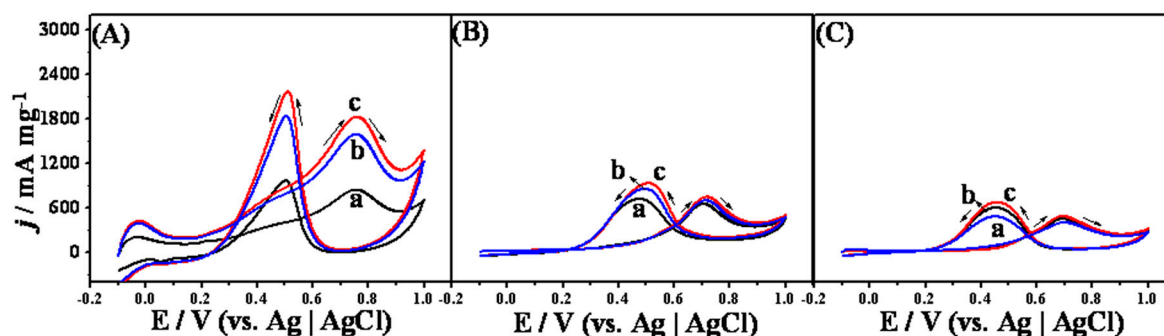


Figure 7. CVs of (A) Pt-Ag/GNs, (B) Pt/GNs and (C) Pt/C-JM in 0.5 M H_2SO_4 + 1.0 M CH_3OH ; curves a, without irradiation; curves b, after visible irradiation for 30 min; curves c, after UV irradiation for 30 min.

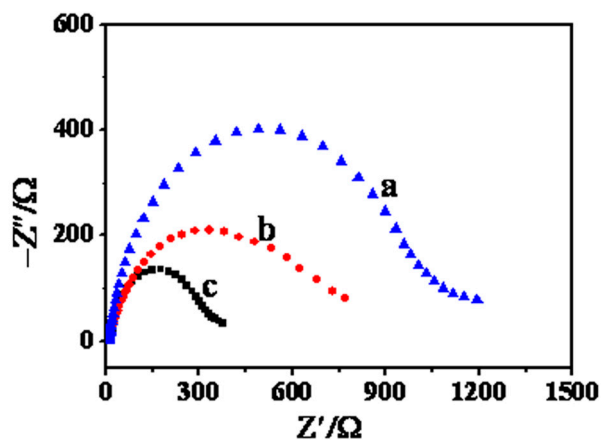


Figure 8. Nyquist plots of Electrochemical Impedance Spectra (EIS) in 0.5 M H_2SO_4 + 1.0 M CH_3OH : Pt/C-JM (a), Pt/GNs (b), and Pt-Ag/GNs (c).

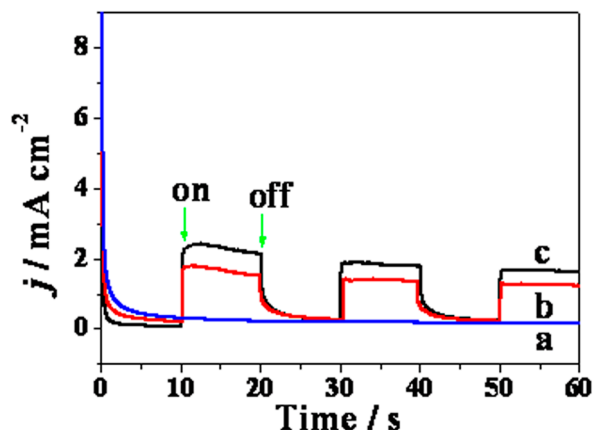


Figure 9. Photocurrent responses of Pt-Ag/GNs: (a) under dark; (b) under intermittent visible irradiation (every 10 s); (c) under intermittent UV irradiation (every 10 s).

The catalytic stability of Pt-Ag/GNs, Pt/GNs, and Pt/C-JM for methanol oxidation was further tested by chronoamperometry in 0.5 M H₂SO₄ containing 1.0 M CH₃OH solution at 0.70 V for 2000 s (Figure 10). As shown in Figure 10, rapid initial current density decay is observed because of CO-like intermediate species (mainly CO_{ads}) poisoning during the methanol electrooxidation reaction [38]. The slower decay slope and the significantly higher final steady-state current density of Pt-Ag/GNs without irradiation (curve c), compared with that of Pt/GNs (curve b) and Pt/C-JM (curve a), indicate that the introduction of Ag into Pt-Ag/GNs improves its electro-catalytic stability for MOR. The enhanced tolerance ability to CO can be reflected in the CO-stripping voltammograms test. As shown in Figure 11, CO-stripping voltammograms of Pt/C-JM (curve a), Pt/GNs (curve b), and Pt-Ag/GNs (curve c) were measured by the oxidation of pre-adsorbed and saturated CO in 0.5 M H₂SO₄ solution at a scan rate of 100 mV·s⁻¹. The peak potential of CO oxidation for Pt-Ag/GNs, Pt/GNs, and Pt/C-JM was 0.67, 0.70 and 0.71 V, respectively. Obviously, Pt-Ag/GNs exhibited a more negative peak potential. The negative shift of the CO oxidation peak demonstrates easier oxidation of CO on the surface of the Pt-Ag/GNs catalyst, indicative of a better anti-poisoning ability. Ag nanoparticles are oxophilic species and can remove the CO-like adsorbing species on Pt active sites at a lower potential through facile formation of Ag(OH)_{ads} [39], contributing to better tolerance towards CO poisoning for Pt-Ag/GNs.

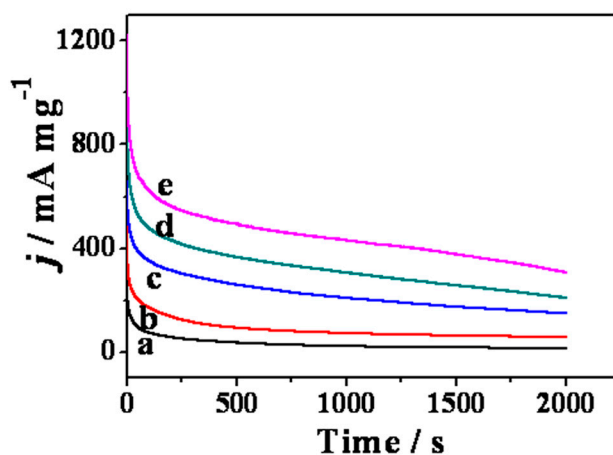


Figure 10. Chronoamperograms in 0.5 M H₂SO₄ + 1.0 M CH₃OH: Pt/C-JM (a), Pt/GNs (b), Pt-Ag/GNs (c), Pt-Ag/GNs under durative visible irradiation (d) and Pt-Ag/GNs under durative UV irradiation (e).

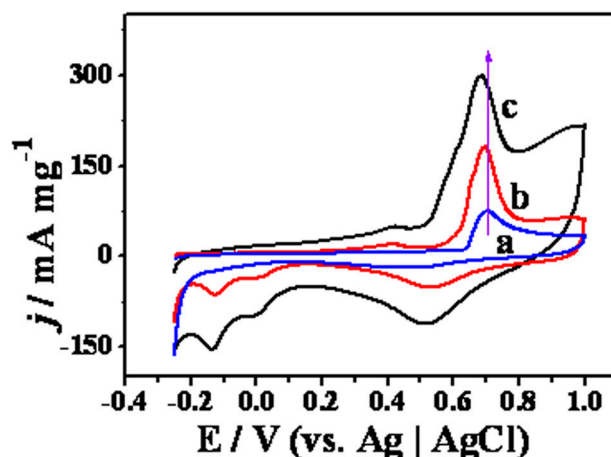


Figure 11. CO-stripping voltammograms of Pt/C-JM (a), Pt/GNs (b), and Pt-Ag/GNs (c) in 0.5 M H_2SO_4 ; scan rate: $100 \text{ mV} \cdot \text{s}^{-1}$.

Particularly, the current density of Pt-Ag/GNs decay more slowly in the presence of light irradiation, and the steady-state current density is significantly enhanced under durative UV (curve e) or visible light irradiation (curve d), which are respectively nearly 2.1 times and 1.4 times higher than that without light irradiation (Figure 10). The results further confirm that the incorporation of Ag brings about the positive effects of light irradiation on the catalytic stability and tolerance to CO poisoning. This is also supported by the ratio of the forward anodic peak current (I_f) to the reverse anodic peak current (I_b) under irradiation. It is well known that the I_f/I_b ratio can also be used to describe the catalyst tolerance to the accumulation of CO-like intermediate species [40–42]. The I_f/I_b of Pt-Ag/GNs is 0.85 after UV irradiation for 30 min, which is higher than that of Pt/GNs (0.80) and Pt/C-JM (0.72) (Figure 7), respectively, implying more valid oxidation of methanol to carbon dioxide during the anodic scan and the removal of poisoning species from the surface of Pt-Ag/GNs under UV irradiation. It should be noted that Pt-Ag/GNs not only exhibited better catalytic activity, stability and tolerance to CO under UV irradiation, but its visible light assisted electro-photo synergistic catalysis performance is also more effective than that of the reported silicon-based Pt-Ag nano-forests catalyst [37]. The efficient synergistic catalysis under UV and visible light irradiation is in favor of harvesting the natural sunlight (UV and visible light) to produce clean energy and provides very promising practical applications. It is well known that noble metal Ag nanoparticles (NPs) show strong visible light absorption due to their surface plasmon resonance (SPR), which is produced by the collective oscillations of surface electrons [43,44]. The unique characteristics of Ag contribute to the beneficial effects of electro-photo-synergistic catalysis under visible light irradiation. Furthermore, GNs can effectively extend the light absorption edge to the visible light region [45]. By integrating with Pt-Ag nanoparticles, GNs are helpful for endowing Pt-Ag/graphene composites with the visible light response for photocatalytic methanol oxidation. Due to the local electromagnetic field and the excellent UV-Visible light absorption capabilities of Ag NPs, the excited electrons can be transferred quickly to GNs, and GNs can be used as the photocatalytic carriers to extract the photo-generated electrons and immediately transfer them to Pt particles, to limit self-photoreduction processes and more easily release Pt active sites [17]. Therefore, the efficient synergistic effects of photo-catalysis and electro-catalysis for MOR are achieved under external light irradiation.

3. Experimental Section

3.1. Materials

Graphite powder (~325 mesh, 99.9995%) was purchased from Alfa Aesar (Ward Hill, Massachusetts, MA, USA). 5% Nafion 117 solution and commercial Pt/C (20%) catalyst (denoted as Pt/C-JM) were

purchased from Johnson Matthey (London, UK). AgNO_3 , $\text{Pt}(\text{NO}_3)_2$, NaOH , KMnO_4 , H_2O_2 (30%), $\text{K}_2\text{S}_2\text{O}_8$, P_2O_5 , H_2SO_4 , acetone, methanol, and ethanol were all analytical reagent and purchased from Sinopharm Chemical Reagent Co., Ltd. (Shanghai, China) and used without further purification. The resistance of deionized water (DI) was 18.2 M Ω .

3.2. Preparation of Pt-Ag/GNs

Graphene oxide (GO) was prepared from purified natural graphite using Hummers' method with some minor modification [46,47]. The product was collected by centrifugation after thoroughly washing with dilute hydrochloric acid and deionized water. After that, the obtained precipitate was dried in vacuum for further use. The overall synthetic route of Pt-Ag/GNs is illustrated in Scheme 1. In a typical synthetic process, 50 mg of GO was dispersed in 50 mL of distilled water by sonication for 30 min. Then, 30 mg of AgNO_3 was added to the mixture under stirring for 30 min. Subsequently, 50 mg of solid sodium hydroxide was added under UV irradiation and the mixture was stirred for another 30 min, which caused that Ag^+ was transformed into Ag_2O [23]. After removing the ultraviolet lamp and adjusting the pH to 7, 3 mL of $\text{Pt}(\text{NO}_3)_2$ (1g/100 mL) were added. After stirring for 30 min, 3 mL of HCOOH (0.5 M) were added. Subsequently, the mixture was stirred for 48 h under ambient condition. After repeated centrifugation (10,000 rpm, 20 min) and thorough washing, the final Pt-Ag/GNs precipitate was lyophilized for 48 h. The counterpart Pt/GNs was prepared by a similar method in the absence of AgNO_3 . The Pt content was determined by inductively coupled plasma atomic emission spectrometry (ICP-AES). The actual loading amount of Pt on the GNs for Pt-Ag/GNs and Pt/GNs was about 20.7 wt % and 25.9 wt %, respectively.

3.3. Characterization Method

The microscopic features and morphology of the samples were investigated through TEM and HRTEM with a TECNAI G2 high-resolution transmission electron microscope (FEI, Hillsboro, Oregon, OR, USA) operating at 200 K. Elemental distribution mapping was performed in a HAADF-STEM with an Oxford INCA energy dispersive X-ray detector (FEI). XPS was conducted on a VG ESCALAB 250 spectrometer (Thermo Scientific, Pleasanton, California, CA, USA) with Al $K\alpha$ radiation (1486.6 eV). XRD patterns were obtained with an X'pert Pro X-ray diffractometer (PANalytical B.V., Holland, The Netherlands), equipped with a Cu $K\alpha$ radiation source. Raman spectra were recorded on a Renishaw-in-Via Raman (Renishaw, London, UK) micro-spectrometer equipped with a 514 nm wavelength laser line. The actual amount of Pt loading in the catalysts was determined by ICP-AES (ICAP6300, Thermo Scientific).

3.4. Electrochemical Measurements

A conventional three electrode cell was used for the electrochemical measurement on a CHI 660C electrochemical workstation (ChenHua, Shanghai, China), with a platinum column as the counter electrode, a standard $\text{Ag} | \text{AgCl}$ (3 M KCl) electrode as the reference, and a modified glassy carbon electrode (GCE, 3.0 mm in diameter) as the working electrode, respectively. To prepare the working electrode, 5 mg of catalyst sample were first dispersed into 1 mL of ethanol by ultrasonication, and then 5 μL of the previously prepared ethanol suspension were dropped onto the pre-cleaned surface of the GCE. Subsequently, an aliquot of Nafion solution (7.5 μL , 0.5%) was dropped on the coated GCE. CVs were recorded in 0.5 M H_2SO_4 or 0.5 M H_2SO_4 solution containing 1.0 M CH_3OH at room temperature with a scan rate of 100 $\text{mV}\cdot\text{s}^{-1}$. CO-stripping voltammograms were performed in a 0.5 M N_2 -saturated H_2SO_4 solution, and then CO was bubbled for 30 min to allow the complete adsorption of CO onto the composites while the working electrode was kept at 0.1 V vs. $\text{Ag} | \text{AgCl}$. Excess CO in the electrolyte was then purged out with N_2 for 15 min. Chronoamperometric curves were obtained for 2000 s in 0.5 M H_2SO_4 solution containing 1.0 M CH_3OH at 0.70 V. EIS was carried out in 0.5 M H_2SO_4 in the presence of 1.0 M CH_3OH with a potential of 0.5 V, and the Nyquist plots were recorded between 0.1 and 100,000 Hz.

3.5. Photo-Electrochemical Measurements

A 15 W UV lamp (ZW3D15WZ105, Cnlight, Guangdong, China) was used to provide UV light ($200 < \lambda < 400$ nm) or visible light ($\lambda > 400$ nm) via different optical filters. It was placed at the bottom of the electrochemical cell, facing the working electrode at a distance of 15 cm. The irradiating power density was measured as $0.3 \text{ mW}\cdot\text{cm}^{-2}$. Cyclic voltammograms and chronoamperometric curve analyses were carried out after external light irradiation for 30 min.

4. Conclusions

In summary, Pt-Ag bimetallic nanoparticles with small size and uniform size distribution were highly dispersed on the surface of GNs in a Pt-Ag/GNs composite with the aid of synchronous reduction by HCOOH. The good dispersion of the Pt-Ag nanoparticles, the strong interaction between the Pt and the Ag nanoparticles, and the good electron transfer capacity of the Pt-Ag/GNs composite contributed to its higher electrocatalytic activity, better tolerance of CO, and better stability for MOR. Under UV or visible light irradiation, Pt-Ag/GNs showed an efficient synergistic photoelectrocatalysis for MOR, which provides an effective strategy to utilize natural sunlight (UV and visible light) to produce clean energy, and favors potential applications of electro-photo catalysts in direct methanol fuel cell anodic reactions.

Acknowledgments: This work was financially supported by the National Natural Science Foundation of China (No. 21171037), and the Research Foundation of the Education Department of Fujian Province (No. JA13082 & No. JB13010).

Author Contributions: Zhongshui Li planned and designed the experiments; Shuhong Xu and Lingting Ye performed the experimental work; Zhongshui Li, Yanli Wang, and Fengling Lei contributed to the data analysis; Shuhong Xu and Lingting Ye wrote the manuscript; Shen Lin supervised the project and the revised manuscript; all authors discussed the results and approved of the final version of the manuscript.

Conflicts of Interest: The authors declare no conflict of interest.

References

1. Jiang, S.P.; Liu, Z.; Hao, L.T.; Mu, P. Synthesis and characterization of PDDA-stabilized Pt nanoparticles for direct methanol fuel cells. *Electrochim. Acta* **2006**, *51*, 5721–5730. [[CrossRef](#)]
2. Yu, L.H.; Xi, J.Y. TiO₂ nanoparticles promoted Pt/C catalyst for ethanol electro-oxidation. *Electrochim. Acta* **2012**, *67*, 166–171. [[CrossRef](#)]
3. Dutta, A.; Ouyang, J.Y. Ternary NiAuPt nanoparticles on reduced graphene oxide as catalysts toward the electrochemical oxidation reaction of ethanol. *ACS Catal.* **2015**, *16*, 1371–1380. [[CrossRef](#)]
4. Bo, Z.; Hu, D.; Kong, J.; Yan, J.H.; Cen, K.F. Performance of vertically oriented graphene supported platinum–ruthenium bimetallic catalyst for methanol oxidation. *J. Power Sources* **2015**, *273*, 530–537. [[CrossRef](#)]
5. Ammam, M.; Easton, E.B. PtCu/C and Pt(Cu)/C catalysts: Synthesis, characterization and catalytic activity towards ethanol electrooxidation. *J. Power Sources* **2013**, *222*, 79–87. [[CrossRef](#)]
6. Guo, J.X.; Sun, Y.F.; Zhang, X.; Tang, L.; Liu, H.T. FePt nanoalloys anchored reduced graphene oxide as high-performance electrocatalysts for formic acid and methanol oxidation. *J. Alloys Compd.* **2014**, *604*, 286–291. [[CrossRef](#)]
7. Hoseini, S.J.; Barzegar, Z.; Bahrami, M.; Roushani, M.; Rashidi, M. Organometallic precursor route for the fabrication of PtSn bimetallic nanotubes and Pt₃Sn/reduced-graphene oxide nanohybrid thin films at oil–water interface and study of their electrocatalytic activity in methanol oxidation. *J. Organomet. Chem.* **2014**, *769*, 1–6. [[CrossRef](#)]
8. Kepeniene, V.; Jablonskiene, J.; Vaiciuniene, J.; Kondrotas, R.; Juskenas, R. Investigation of graphene supported platinum-cobalt nanocomposites as electrocatalysts for ethanol oxidation. *J. Electrochem. Soc.* **2014**, *59*, 135–136.
9. Shen, Y.; Zhang, M.Z.; Xiao, K.J.; Xi, Z.Y. Synthesis of Pt, PtRh, and PtRhNi alloys supported by pristine graphene nanosheets for ethanol electrooxidation. *ChemCatChem* **2014**, *6*, 3254–3261. [[CrossRef](#)]

10. Lu, Y.Z.; Jiang, Y.T.; Wu, H.B.; Wei, C. Nano-PtPd cubes on graphene exhibit enhanced activity and durability in methanol electrooxidation after CO stripping-cleaning. *J. Phys. Chem. C* **2013**, *117*, 2926–2938. [[CrossRef](#)]
11. Li, L.Z.; Chen, M.X.; Huang, G.B.; Yang, N.; Zhang, L.; Wang, H.; Liu, Y.; Wang, W.; Gao, J.P. A green method to prepare Pd–Ag nanoparticles supported on reduced graphene oxide and their electrochemical catalysis of methanol and ethanol oxidation. *J. Power Sources* **2014**, *263*, 13–21. [[CrossRef](#)]
12. Kale, M.J.; Avanesian, T.; Christopher, P. Direct photocatalysis by plasmonic nanostructures. *ACS Catal.* **2013**, *4*, 116–128. [[CrossRef](#)]
13. Hou, W.B.; Cronin, S.B. A review of surface plasmon resonance-enhanced photocatalysis. *Adv. Funct. Mater.* **2013**, *23*, 1612–1619. [[CrossRef](#)]
14. Gao, L.N.; Yue, W.B.; Tao, S.S.; Fan, L.Z. Novel strategy for preparation of graphene-Pd, Pt composite, and its enhanced electrocatalytic activity for alcohol oxidation. *Langmuir* **2012**, *29*, 957–964. [[CrossRef](#)] [[PubMed](#)]
15. Sun, Y.Q.; Wu, Q.; Shi, G.Q. Graphene based new energy materials. *Energy Environ. Sci.* **2011**, *4*, 1113–1132. [[CrossRef](#)]
16. Lei, F.L.; Li, Z.S.; Ye, L.T.; Wang, Y.L.; Lin, S. One-pot synthesis of Pt/SnO₂/GNs and its electro-photo-synergistic catalysis for methanol oxidation. *Int. J. Hydrogen Energy* **2015**, *41*, 255–264. [[CrossRef](#)]
17. Ye, L.T.; Li, Z.S.; Zhang, L.; Lei, F.L.; Lin, S. A green one-pot synthesis of Pt/TiO₂/Graphene composites and its electro-photo-synergistic catalytic properties for methanol oxidation. *J. Colloid Interface Sci.* **2014**, *433*, 156–162. [[CrossRef](#)] [[PubMed](#)]
18. Zhang, H.L.; Hu, C.G.; He, X.S.; Liu, H.; Du, G.J.; Zhang, Y. Pt support of multidimensional active sites and radial channels formed by SnO₂ flower-like crystals for methanol and ethanol oxidation. *J. Power Sources* **2011**, *196*, 4499–4505. [[CrossRef](#)]
19. Wen, Z.L.; Yang, S.D.; Liang, Y.Y.; Wei, H.; Hao, T.; Liang, H.; Zhang, X.G.; Song, Q.J. The improved electrocatalytic activity of palladium/graphene nanosheets towards ethanol oxidation by tin oxide. *Electrochim. Acta* **2010**, *56*, 139–144. [[CrossRef](#)]
20. Ma, S.S.; Xue, J.J.; Zhou, Y.M.; Zhang, Z.W. Photochemical synthesis of ZnO/Ag₂O heterostructures with enhanced ultraviolet and visible photocatalytic activity. *J. Mater. Chem. A* **2014**, *2*, 7272–7280. [[CrossRef](#)]
21. Li, S.S.; Lv, J.J.; Hu, Y.Y.; Zheng, J.N.; Chen, J.R.; Wang, A.J.; Feng, J.J. Facile synthesis of porous Pt–Pd nanospheres supported on reduced graphene oxide nanosheets for enhanced methanol electrooxidation. *J. Power Sources* **2014**, *247*, 213–218. [[CrossRef](#)]
22. Zhang, L. A facile synthesis of flower-shaped TiO₂/Ag microspheres and their application in photocatalysts. *RSC Adv.* **2014**, *4*, 54463–54468. [[CrossRef](#)]
23. Sarkar, D.; Ghosh, C.K.; Mukherjee, S.; Chattopadhyay, K.K. Three dimensional Ag₂O/TiO₂ type-II (p–n) nanoheterojunctions for superior photocatalytic activity. *ACS Appl. Mater. Interfaces* **2013**, *5*, 331–337. [[CrossRef](#)] [[PubMed](#)]
24. Wang, S.L.; Qian, H.H.; Hu, Y.; Dai, W.; Zhong, Y.J.; Chen, J.F.; Hu, X. Facile one-pot synthesis of uniform TiO₂-Ag hybrid hollow spheres with enhanced photocatalytic activity. *Dalton Trans.* **2013**, *42*, 1122–1128. [[CrossRef](#)] [[PubMed](#)]
25. Cao, J.Y.; Guo, M.W.; Wu, J.Y.; Xu, J.; Wang, W.C.; Chen, Z.D. Carbon-supported Ag@Pt core–shell nanoparticles with enhanced electrochemical activity for methanol oxidation and oxygen reduction reaction. *J. Power Sources* **2015**, *277*, 155–160. [[CrossRef](#)]
26. Ganesan, P.; Prabu, M.; Sanetuntikul, J.; Shanmugam, S. Cobalt sulfide nanoparticles grown on nitrogen and sulfur codoped graphene oxide: An efficient electrocatalyst for oxygen reduction and evolution reactions. *ACS Catal.* **2015**, *5*, 3625–3637. [[CrossRef](#)]
27. Kim, Y.; Shanmugam, S. Polyoxometalate-reduced graphene oxide hybrid catalyst: Synthesis, structure, and electrochemical properties. *ACS Appl. Mater. Interfaces* **2013**, *5*, 12197–12204. [[CrossRef](#)] [[PubMed](#)]
28. Graf, D.; Molitor, F.; Ensslin, K.; Stampfer, C.; Jungen, A.; Hierold, C.; Wirtz, L. Spatially resolved raman spectroscopy of single- and few-layer graphene. *Nano Lett.* **2007**, *7*, 238–242. [[CrossRef](#)] [[PubMed](#)]
29. Routh, P.; Das, S.; Shit, A.; Bairi, P.; Das, P.; Nandi, A.K. Graphene quantum dots from a facile sono-fenton reaction and its hybrid with a polythiophene graft copolymer toward photovoltaic application. *ACS Appl. Mater. Interfaces* **2013**, *5*, 12672–12680. [[CrossRef](#)] [[PubMed](#)]
30. Liu, X.W.; Duan, J.L.; Chen, H.L.; Zhang, Y.F.; Zhang, X.L. A carbon riveted Pt/graphene catalyst with high stability for direct methanol fuel cell. *Microelectron. Eng.* **2013**, *110*, 354–357. [[CrossRef](#)]

31. Yan, Y.; Wei, W.; Liu, Y.Q.; Wang, F.X.; Zhe, Z.; Lei, Z.Q. Carbon supported heterostructured Pd–Ag nanoparticle: Highly active electrocatalyst for ethylene glycol oxidation. *Int. J. Hydrogen Energy* **2015**, *40*, 2225–2230.
32. Wang, J.J.; Yin, G.P.; Zhang, J.; Wang, Z.B.; Gao, Y.Z. High utilization platinum deposition on single-walled carbon nanotubes as catalysts for direct methanol fuel cell. *Electrochim. Acta* **2007**, *52*, 7042–7050. [[CrossRef](#)]
33. Yang, C.Z.; Laak, N.K.v.d.; Chan, K.Y.; Zhang, X. Microwave-assisted microemulsion synthesis of carbon supported Pt–WO₃ nanoparticles as an electrocatalyst for methanol oxidation. *Electrochim. Acta* **2012**, *75*, 262–272. [[CrossRef](#)]
34. Huang, H.L.; Liu, Y.J.; Gao, Q.Z.; Ruan, W.S.; Lin, X.M.; Xin, L. Rational construction of strongly coupled metal–metal oxide–graphene nanostructure with excellent electrocatalytic activity and durability. *ACS Appl. Mater. Interfaces* **2014**, *6*, 10258–10264. [[CrossRef](#)] [[PubMed](#)]
35. Maiyalagan, T.; Alaje, T.O.; Scott, K. Highly stable Pt–Ru nanoparticles supported on three-dimensional cubic ordered mesoporous carbon (Pt–Ru/CMK-8) as promising electrocatalysts for methanol oxidation. *J. Phys. Chem. C* **2012**, *116*, 2630–2638. [[CrossRef](#)]
36. Kashyout, A.B.; Bakr, A.; Nassr, A.B.A.A.; Giorgi, L.; Maiyalagan, T.; Youssef, B.A.B. Electrooxidation of methanol on carbon supported Pt–Ru nanocatalysts prepared by ethanol reduction method. *Int. J. Electrochem. Sci.* **2011**, *6*, 379–393.
37. Lin, C.T.; Shiao, M.H.; Chang, M.N.; Chu, N.; Chen, Y.W.; Peng, Y.H.; Liao, B.H.; Huang, H.J.; Hsiao, C.N.; Tseng, F.G. A facile approach to prepare silicon-based Pt–Ag tubular dendritic nano-forests (tDNFs) for solar-light-enhanced methanol oxidation reaction. *Nanoscale Res. Lett.* **2015**, *10*, 1–8. [[CrossRef](#)] [[PubMed](#)]
38. Li, Z.S.; Huang, X.M.; Zhang, X.F.; Zhang, L.; Lin, S. The synergistic effect of graphene and polyoxometalates enhanced electrocatalytic activities of Pt–{PEI-GNs/[PMo₁₂O₄₀]^{3–}}_n composite films regarding methanol oxidation. *J. Mater. Chem.* **2012**, *22*, 23602–23607. [[CrossRef](#)]
39. Zheng, J.N.; Lv, J.J.; Li, S.S.; Xue, M.W.; Wang, A.J.; Feng, J.J. One-pot synthesis of reduced graphene oxide supported hollow Ag@Pt core-shell nanospheres with enhanced electrocatalytic activity for ethylene glycol oxidation. *J. Mater. Chem.* **2014**, *2*, 3445–3451. [[CrossRef](#)]
40. Maiyalagan, T.; Dong, X.C.; Chen, P.; Wang, X. Electrodeposited Pt on three-dimensional interconnected graphene as a free-standing electrode for fuel cell application. *J. Mater. Chem.* **2012**, *22*, 5286–5290. [[CrossRef](#)]
41. Maiyalagan, T. Pt–Ru nanoparticles supported PAMAM dendrimer functionalized carbon nanofiber composite catalysts and their application to methanol oxidation. *J. Solid State Electrochem.* **2009**, *13*, 1561–1566. [[CrossRef](#)]
42. Sanetuntikul, J.; Ketpang, K.; Shanmugam, S. Hierarchical nanostructured Pt₈Ti–TiO₂/C as an efficient and durable anode catalyst for direct methanol fuel cells. *ACS Catal.* **2015**, *5*, 7321–7327. [[CrossRef](#)]
43. Guo, R.; Zhang, G.K.; Liu, J. Preparation of Ag/AgCl/BiMg₂VO₆ composite and its visible-light photocatalytic activity. *Mater. Res. Bull.* **2013**, *48*, 1857–1863. [[CrossRef](#)]
44. Jin, R.; Cao, Y.; Mirkin, C.A.; Kelly, K.L.; Schatz, G.C.; Zheng, J.G. Photoinduced conversion of silver nanospheres to nanoprisms. *Science* **2001**, *294*, 1901–1903. [[CrossRef](#)] [[PubMed](#)]
45. Liu, Y.P.; Fang, L.; Lu, H.D.; Li, Y.W.; Hu, C.Z.; Yu, H.G. One-pot pyridine-assisted synthesis of visible-light-driven photocatalyst Ag/Ag₃PO₄. *Appl. Catal. B* **2012**, *115–116*, 245–252. [[CrossRef](#)]
46. Kovtyukhova, N.I.; Ollivier, P.J.; Martin, B.R.; Mallouk, T.E.; Chizhik, S.A.; Buzaneva, E.V.; Gorchinskiy, A.D. Layer-by-layer assembly of ultrathin composite films from micron-sized graphite oxide sheets and polycations. *Chem. Mater.* **1999**, *11*, 771–778. [[CrossRef](#)]
47. Zeng, Q.; Cheng, J.S.; Tang, L.H.; Liu, X.F.; Liu, Y.Z.; Li, J.H.; Jiang, J.H. Self-assembled graphene–enzyme hierarchical nanostructures for electrochemical biosensing. *Adv. Funct. Mater.* **2010**, *20*, 3366–3372. [[CrossRef](#)]

